A Discrete Damage Mechanics Model for Fatigue of MEMS Devices

Trevor Slack
Ph.D. Research Assistant
School of Mechanical Engineering

Farshid Sadeghi,
Professor
School of Mechanical Engineering

Dimitrios Peroulis
Assistant Professor
School of Electrical and Computer Engineering

Purdue University
West Lafayette, IN 47906, USA

Abstract

Fatigue initiation and failure of various MEMS is of significant importance as they gain widespread acceptance in sensors and electronics. This paper presents an approach for utilizing available experimental fatigue data to evaluate the fatigue lives of MEMS components. The approach is based upon a discontinuous material representation and continuum damage mechanics principles. The presented model utilizes experimental data measured over just a few millions of cycles to predict the fatigue life for more than a trillion cycles. This is particularly critical for MEMS since measurements that last several hundreds of billions of cycles require many months or years to complete. Furthermore, the proposed model captures the statistical distribution of material properties and geometrical randomness of the microstructure commonly observed in a wide variety of MEMS. Consequently, simulations that account for the variability in fatigue life can be readily performed even for fatigue lives that exceed a trillion cycles. The discrete element model developed is applied to a dog-bone shaped tensile specimen to evaluate the influence of material heterogeneity and material flaws on fatigue crack initiation life and scatter. The ability of the model to predict the fatigue life of different types of MEMS devices and loading conditions is also demonstrated.

Keywords: MEMS, Fatigue, Discrete Element Method, Damage Mechanics

Introduction

The applications of Micro Electro Mechanical Systems (MEMS) are continuously growing. The successful development of a device requires both the experimental determination of the relevant material properties as well as modeling techniques that can capture heterogeneous effects caused by the material microstructure. In many applications such as accelerometers [1], angular rate sensors [2] and RF MEMS switches and varactors [3] components are subjected to cyclically varying loads and are expected to withstand billions or trillions of loading cycles. In other applications the MEMS device may be subjected to unwanted machine vibrations. For this reason it is important to understand the fatigue behavior of materials used in MEMS devices.

The mechanical performance of materials used in MEMS devices depends both on the fabrication process and post-processing [4]. Thus to accurately measure the mechanical properties of MEMS devices experiments have to be performed on micron-scale specimens. Much of the work in fatigue characterization has been conducted for polysilicon due to its predominant use as a structural material for MEMS. Various approaches have been attempted using both integrated and external actuation of specimens in bending and tension [5] - [8]. A review of the test devices developed as well as a comparison of the experimental data obtained by different research groups for polysilicon has been compiled by Sharpe et al. [9]. The results presented by Sharp et al. [9] show significant discrepancy between the results from different groups and a large amount of scatter in the results for each group. Several fatigue mechanisms have been proposed including stress-assisted surface oxide dissolution, reaction layer fatigue, and mechanically induced subcritical cracking [10].

Significant work has also been done to characterize the fatigue behavior of LIGA Ni [11] - [13]. Yang et al. [13] performed tensile testing of samples composed of both columnar and nano-scale grains. Depending on the thickness of the samples with columnar grains fatigue behavior was observed to be similar to either annealed Ni or wrought Ni. A significant strengthening of fatigue resistance was found for the samples with nano-scale grains. The

samples with columnar grains showed evidence of persistent slip bands at which cracks were often found to nucleate. For the nanostuctured samples, cracks were found to nucleate from pre-existing surface and corner defects. Aktaa et al. [12] also performed direct tensile testing of LIGA Ni. By extending their results to the fully reversed loading condition they also found a good comparison with fatigue properties of bulk Ni.

This paper presents a modeling approach which utilizes available experimental results in a way that allows for the stochastic fatigue modeling of MEMS devices. The model is based on the theory of damage mechanics [14] - [16] and explicitly takes into account the gradual material degradation that occurs under cyclic loading. The methodology consists of solving the coupled damage evolution and material constitutive equations in a discrete material framework that accounts for the stochastic nature of the material microstructure and properties. The model is applied to a dog-bone shaped tensile specimen to evaluate the influence of various material parameters and randomness of grain boundary structure on fatigue scatter. The model is also used to investigate the effects of material flaws by demonstrating the influence of a random initial crack on fatigue life.

Discrete Element Material Representation

The analysis presented in this investigation is based on a discrete material representation. The method differs from the standard numerical techniques such as the finite element method where a domain is discretized into smaller sub-domains in order to integrate the governing equations derived from continuum mechanics. In the discrete element method (DEM) a domain is composed of smaller sub-domains that interact with one another through contact at their boundaries. This is illustrated in Figure 1 which shows a material domain that is composed of numerous interacting micro-elements which represent in this case the grains of the material. Each element is a rigid body with two translational degrees of freedom and one rotational degree of freedom. The elements are connected along their lines of intersection with a continuous set of

fibers. As shown in Figure 2(a) as one element moves relative to another the fibers connecting the two elements are stretched. The stretching of the fiber results in forces between the two elements. As shown in Figure 2(b) the forces are decomposed into normal and tangential components and are given both elastic and viscous properties. For the current study only elastic effects are considered with fiber stiffnesses, K_n in the normal direction and K_t in the tangential direction, that are related to the macroscopic elastic properties E (modulus of elasticity) and ν (Poisson's ratio) [17]. The interaction of an element with all of its neighbors' results in an equivalent force $\boldsymbol{F}$ and moment $\boldsymbol{M}$ being applied to the elements center of mass. The solution of a given boundary value problem consists of specifying the time dependant boundary conditions and the simultaneous integration of the equations of motion for all the elements in the domain. Further details of the element interaction and the method by which stresses are extracted can be found in [17] - [18].

The grains of a polycrystalline material can be represented to a good degree of accuracy through the process of Voronoi tessellation [19] - [20]. This process consists of using a set of randomly placed points as nucleation points or seeds and constructing regions around them such that all points enclosed by the region are closer to the given nucleation point than any other nucleation point. The process results in a set of convex polygons known as Voronoi polygons. The randomly placed nucleation points lead to a non-unique material domain for every tessellation simulation. This produces topological randomness in the simulated microstructures. In the present model, the micro-elements are taken to be material grains that are generated through such a Voronoi tessellation process. The size of the grains is controlled by specifying the density of the nucleation points. The generated element shapes have variable number of sides and variable orientations. The most probable number of sides is six, which also corresponds to the number of sides for maximum thermodynamic stability of material grains. Care is taken during

the tessellation process to obtain uniformity of the grain size by setting upper and lower limits on the distances between the nucleation points.

Fatigue Damage Modeling

Damage mechanics is concerned with the progressive deterioration of a material due to the initiation and growth of micro-cracks and voids [14] - [16], [21]. The initiation and early growth of damage is discontinuous and is strongly affected by the heterogeneous nature of polycrystalline materials [22]. The effects of damage on the mechanical response of a material are captured through the introduction of a damage variable ***D*** into the constitutive equations. In general the damage variable is a tensor but under the assumption of isotropic damage it reduces to a scalar variable *D*. A one dimensional damaged coupled elasticity law takes the form

$$\sigma = (1 - D)E\varepsilon \tag{1}$$

where the value of *D* ranges from zero for an undamaged material to one for a completely damaged material. A value of one corresponds to a complete loss of stiffness in tension signifying crack initiation.

Constitutive equations for the evolution of the damage variable have been formulated within the framework of thermodynamics for fatigue damage, ductile damage, and creep damage [21]. In high cycle fatigue a commonly used form for the evolution of D is [23] - [26]

$$\frac{dD}{dN} = \left[\frac{\Delta\sigma}{\sigma_r(\sigma_m)(1 - hD)} \right]^m \tag{2}$$

where *N* is the cycle number, $\Delta\sigma$ is the stress range, σ_m is the mean stress, σ_r and *m* are temperature dependent material parameters that have to be experimentally identified, and *h* is a crack closure parameter. The crack closure parameter is introduced to capture the effects of the partial closing of micro-cracks that occur in compression. The value of *h* is one in tension and following Lemaitre [21] is taken as 0.2 in compression. Note that σ_r which is a function of the

mean stress is also referred to as the resistance stress [26], so called because it is the parameter that controls an elements ability to resist damage accumulation. The damage variable is implemented within the current modeling framework through the reduction of the fiber stiffness components as

$$\begin{aligned} \left(K_n\right) &= \left(K_n\right)^0 \left(1-D\right) \\ \left(K_t\right) &= \left(K_t\right)^0 \left(1-D\right) \end{aligned} \tag{3}$$

where $\left(K_n\right)^0$ and $\left(K_t\right)^0$ are the initial normal and tangential stiffness components. The effect of damage on the normal stress-strain relationship for a particular joint, including the crack closure effect, is illustrated in Figure 3.

Numerical Solution of the Damaged Coupled Equations

The fatigue simulation is carried out by applying Equation (2) locally to every element to element fiber set within the material domain. Solution of the resulting system of coupled first order differential equations requires knowledge of the stress range $\Delta\sigma$ in every fiber set as a function of the fatigue cycle *N*. Since high cycle fatigue involves millions of cycles a fully coupled analysis using the material model is impossible and a compromise has to be made. The procedure adopted here is referred to as the 'jump-in-cycles' method and is outlined by Lemaitre [21].

The method assumes a piecewise periodic loading that is constant over a number of cycles N^i during which the damage of all the inter-element joints is known to be D_j^i where *j* ranges over the number of joints in the domain and *i* indicates a block of cycles. The material model is used to determine the stress range $\Delta\sigma_j^i$ in the joints and the damage evolution rate in each joint is given by

$$\left(\frac{dD}{dN}\right)_j^i = \left[\frac{\Delta\sigma_j^i}{\sigma_r(1-hD_j^i)}\right]^m . \tag{4}$$

The increment in damage ΔD is assumed to be constant over the block of cycles so the number of cycles in the current block of cycles is computed as

$$\Delta N^i = \frac{\Delta D}{\left(\frac{dD}{dN}\right)_{crit}^i} \tag{5}$$

where

$$\left(\frac{dD}{dN}\right)_{crit}^i = Max\left|\left(\frac{dD}{dN}\right)_j^i\right| \tag{6}$$

is the joint with the maximum damage evolution rate. The number of cycles is updated as

$$N^{i+1} = N^i + \Delta N^i \tag{7}$$

and the damage at each joint is updated using

$$D_j^{i+1} = D_j^i + \left(\frac{dD}{dN}\right)_j^i \Delta N^i . \tag{8}$$

The joint fiber stiffnesses are updated according to Equation (3) and the procedure is repeated for the next block of cycles. The value of the damage increment ΔD has to be chosen large enough to allow a reasonable computational time but small enough so that the coupling between damage and stress is not violated. The piecewise linear growth in damage produced by the procedure is illustrated in Figure 4.

Identification of Material Fatigue Parameters

As described earlier the fatigue damage evolution equation introduces two new material parameters that have to be experimentally determined. The method used here is to identify the parameters from experimental stress-life data (S-N curve) available in the literature. Buchheit et

al. [11] performed fully reversed, R = -1, evaluation of LIGA Ni samples. Their experimental results are shown in Figure 5. Also shown is a power law fit of the data of the form

$$\Delta\sigma = AN^{B} \tag{9}$$

where σ_a is the stress amplitude. Using the least squares method the curve fit parameters to the experimental results are determined to be

$$A = 2063MPa \ , B = -0.112. \tag{10}$$

A comparison is made with the damage evolution equation by assuming that there is no coupling between the damage and stress level and taking the micro-crack closure parameter to be one in both tension and compression. Under these conditions Equation (2) can be integrated from the undamaged to completely damaged states giving

$$\int_0^{N_f} dN = \int_0^1 \left\{ \frac{\sigma_r (1-D)}{\Delta\sigma} \right\}^m dD \quad \Rightarrow \ N_f = \frac{1}{(m+1)} \left[\frac{\sigma_r}{\Delta\sigma} \right]^m \tag{11}$$

where N_f is the number of cycles to failure at the stress level $\Delta\sigma$. Rearranging Equation (11) gives

$$\Delta\sigma = \sigma_r (m+1)^{-\frac{1}{m}} N^{-\frac{1}{m}}. \tag{12}$$

Comparison with Equations (9) and (10) gives the fatigue material parameters as

$$m = 8.93 \ , \sigma_r = 2668 \ MPa. \tag{13}$$

Application of the Model to a Tensile Specimen

The damage mechanics based fatigue model is applied to a dog-bone shaped fatigue specimen to predict the stress life behavior and to investigate the influence of various material parameters and process induced material flaws on fatigue scatter. Figure 6 illustrates the dimensions of the simulated specimen. Tensile specimens of similar shape and dimension have been produced using micro-machining techniques by several research groups [27] - [30] for

fatigue testing by external actuation. Table 1 contains the parameters used in this investigation. Fifty material domains were generated using the Voronoi tessellation process to evaluate the statistical nature of the fatigue phenomena. The boundary conditions imposed on the specimen are that the x displacement degrees of freedom on one end are fixed while the x displacement degrees of freedom on the other end are specified such that the desired stress amplitude is obtained in the straight section of the specimen. It is assumed that the fatigue behavior is governed by the normal stress component acting on the element boundaries. To reduce the computational effort for the statistical and stress life investigations of the tensile specimen the simulations were performed only up to the condition of crack initiation. This is warranted in light of the fact that much of the scatter that occurs in fatigue data can be attributed to the initiation and early growth of fatigue cracks [22] and also due to the fact that in the case of high cycles fatigue much of the life is spent in the crack initiation stage [31].

Shown alongside the experimental data and curve fit in Figure 5 are the analytical results obtained using the model under the assumption of uniform material properties (E, ν, σ_r and m). At each stress level simulations were performed using ten domains. Under the assumption of uniform material properties the only source of randomness is topological randomness due to the geometrical variations in the microstructures produced using the Voronoi tessellation process. As can be seen from Figure 5 this source of randomness alone has very little effect on the scatter in the fatigue data. Note however that there is good agreement between the simulated and experimental results.

Table 1: Simulation Parameters

Elastic modulus of material (E)	175 GPa
Poisson's ratio ν	0.31
Tensile Strength	550 MPa
Mean Element size	13 μm
Damage increment (ΔD)	0.02
Stress amplitude σ_a	200 MPa
Stress ratio R = $\sigma_{\max} / \sigma_{\min}$	-1

Effect of Material Inhomogeneity on Fatigue Life

Inhomogeneous material behavior can result from geometrical variations in the microstructure, grain anisotropy and spatially distributed material properties. To investigate the effects of material inhomogeneity on fatigue life three sources will be considered independently. The conditions to be investigated are homogenous material properties, variable elastic modulus and variable resistance stress. For each condition fifty domains are subjected to a maximum stress of 200 MPa under completely reversed loading conditions until a crack initiates.

Homogenous Material Properties: In this case, the material elastic and damage properties (E, ν, σ_r and m) are held constant throughout the domain. This condition isolates the variability between the domains to that of the microstructural randomness that occurs as a result of the Voronoi tessellation process. The results for this condition are shown on a Weibull probability plot in Figure 7. The Weibull slope is 12.94 and the Weibull strength, indicating the number of cycles for which the probability of failure is 63.2%, is 2,626,567 (cycles). The large value of the Weibull slope indicates that there is very little scatter in the results.

Variable Elastic Modulus: For the second condition the elastic modulus is assumed to vary spatially throughout the domain. This condition is implemented by treating the elastic modulus as a random variable and sampling each of the individual joint stiffnesses K_n and K_t from a normal distribution centered at a mean modulus of 175 (GPa) and with a standard deviation of 5.83 (GPa). The other material properties (ν, σ_r and m) are held constant. This condition will

create local stress concentrations in the domain due to the interaction of elements with different stiffnesses. The results are shown in Figure 7. The data fall in a straight line indicating adherence to a Weibull distribution. The Weibull slope of the data is 7.61 and the Weibull strength is 2,173,140 (cycles). The lower values of the Weibull slope and Weibull strength indicate an increase in scatter and a reduction in the fatigue life as compared with the homogenous property condition.

Variable Resistance Stress: For the final condition a spatially distributed value of resistance stress, σ_r, is considered. This condition is implemented in the model by sampling the resistance stress term for each inter-element joint from a Normal distribution with a mean of 2668 (GPa) and a standard deviation of 89 (GPa). The other material properties (E, ν, and m) are held constant. The results for this condition are also shown in Figure 7. Again, the data follows a straight line. The Weibull slope of the data is 8.58 and the Weibull strength is 1,755,693 (cycles). This condition leads to a nearly identical increase in scatter as was found for the variable elastic modulus condition. As expected, a larger reduction in fatigue life results for this condition, because the resistance stress variable relates directly to the fatigue strength of the elements.

Effect of Material Flaws on Fatigue Life

Flaws in MEMS components can be produced both during fabrication and post-processing. During fabrication voids and or weak bonds can form between neighboring grains. During etching processes overetch can lead to undercuts and/or surface flaws. For the case of polysilicon material work has been conducted to characterize the critical flaw size and location in the context of brittle failure [32] - [35]. These same flaw populations can act as sites of stress concentration where fatigue crack initiation is likely to occur. In this section, the effects of three types of initial material flaws on fatigue life are considered. For each type of flaw, life data was obtained for fifty domains under the loading conditions considered previously.

Initially Broken Intergranular Bond: The first type of flaw considered was an initially broken intergranular bond. This flaw is implemented in the model by randomly selecting a joint within the straight section of the dog-bone and assigning it an initial damage value of one. A joint with a damage value of one will have no stiffness in tension and a reduced stiffness in compression over that of the surrounding material. Uniform material properties are assumed. The distribution of Von Mises stress around an initially broken bond, represented by a black line, for one of the specimens is shown in Figure 8. Thee stress concentration caused by the flaw can be clearly seen in Figure 8. The crack initiation lives are shown on a Weibull probability plot in Figure 9. The Weibull slope of the data is 3.21 and the Weibull strength is 2,125,316 (cycles). The Weibull slope indicates a much larger increase in scatter than resulted for each of the variable material property cases. However, the Weibull strength falls between those that resulted for the conditions of variable elastic modulus and variable resistance stress.

Internal Void: The second type of flaw considered was an internal void within the domain. This is implemented in the model by randomly removing one element from the interior of straight section of each domain. The distribution of Von Mises stress around the internal void for one of the domains is shown in Figure 10. The crack initiation lives are shown on a Weibull probability plot in Figure 9. The Weibull slope of the data is 1.12 and the Weibull strength is 133,009 (cycles). This condition leads to a large increase in scatter and to a large decrease in the Weibull strength.

Surface Void: The final type of material flaw that will be considered is an initial surface void as might result from non-perfect wet or dry etching [36]. This is implemented in the model by randomly removing one element from the surface of the straight section of each specimen. The distribution of Von Mises stress around a surface void for one of the domains is shown in Figure 11. The crack initiation lives are shown on a Weibull probability plot in Figure 9. The Weibull slope of the data is 0.71 and the Weibull strength is 11,266 (cycles). This condition leads to the

largest increase in scatter and largest decrease in Weibull strength of all the conditions considered.

The Weibull statistics for all of the material property and flaw cases are summarized in Table 2. Material property variation led to a slight increase in scatter and also to a slight decrease in the Weibull strength. The results were similar for both the variable elastic modulus and variable resistance stress conditions. The initial broken intergranular bond condition led to a larger increase in scatter but to a decrease in Weibull strength that was similar to the variable material property conditions. The most critical effects were seen for the initial internal and surface voids which both led to a large reduction in the Weibull strength indicating a significantly lower fatigue life. Please note that for the material flaw cases, particularly the initial surface void case, the results don't follow a straight line indicating that the two parameter Weibull distribution is not the best fit and perhaps a three parameter Weibull distribution should be considered.

Table 2: Weibull Probability Statistics

Simulation Condition	Weibull Slope, e	Weibull Strength (cycles)
Homogenous	12.94	2626567
Variable Modulus	7.61	2173140
Variable Resistance Stress	8.58	1755693
Initial broken intergranular bond	3.21	2125316
Initial internal void	1.12	133009
Initial surface void	0.71	11266

Effect of Material Flaws on Stress Life Behavior

The previous simulations have all been performed at a single stress level so that some characteristics of the statistical behavior could be described. Also of interest to the MEMS designer is the fatigue behavior of a component over a range of stresses. To capture this behavior simulations are performed at five different stress levels so that a stress-life curve can be obtained. Three stress-life results are produced corresponding to each of the three types of initial flaws considered previously. For each initial flaw condition ten domains with uniform material

properties were used at each stress level. As was shown in Figures 8, 10 and 11 each type of initial flaw led to a stress concentration in the domain. Depending upon the stress level and the severity of the stress concentration static failure could occur. To check for static failure the normal stress in each joint is first compared against the static strength of the material, listed in Table 1, before the damage evolution equation is applied. If the stress in any joint exceeds the tensile strength of the material the joint is assumed to break under static conditions.

The stress life results corresponding to each of the initial flaw conditions are displayed in Figures 12 through 14. Also shown, for comparison purposes is the stress life results for the ten domains used for each condition in the absence of the flaw considered. Figure 12 shows the stress life curve for the initial broken intergranular bond. The data follows very closely the flaw free condition with some overlap in the data occurring at each stress level. At the highest stress level, 400 (*MPa*), two of the domains failed statically. Figure 13 shows the stress life results for the case of an initial internal void. Much more scatter can be seen in the data compared to the initial broken bond case. At the highest stress level seven of the domains failed statically. Figure 14 shows the stress life results corresponding to the condition of an initial surface void. This condition led to the largest increase in scatter, the largest decrease in life and to the most domains failing statically. At the highest stress level all ten domains failed statically. At a stress of 300 (*MPa*) six of the domains failed statically and at a stress of 200 (*MPa*) one domain failed statically.

For each of the stress life results developed a power law fit is made through the mean of the life data that did not fail statically at each stress level. For each condition the slope of the power law curve was within five percent of that of that given for the experimental data in Equation 10. The results indicate the deleterious effects caused by the initial flows which lead to both a reduction in the overall life and to an increase in scatter in the data. For the surface void condition the fatigue life at the lower stress levels is spread out over more than two orders of magnitude of cycles.

Predicting the Life of a MEMS Resonator

The previous simulations were performed for the simple stress state of uniform tension. MEMS structures are varied and are subjected to many different states of stress. One common structure, depicted in Figure 15, consists of a membrane suspended above a substrate by supporting beams. Such a structure might be found in application as a MEMS resonator, variable capacitor or accelerometer [37] - [38]. Simulations were performed to determine the life of one of the supporting beams as it is subjected to cyclically varying loads due to the motion of the membrane. The material properties listed in Table 1 will again be used. The dimensions of the supporting beam are given in Figure 16. The boundary conditions imposed on the beam are that one end is fixed while at the other end all of the elements are given an equivalent displacement in the *y* direction. The distribution of Von Mises stress that is developed in the beam due to these boundary conditions is shown in Figure 16. Bending stresses are developed in both the horizontal and vertical sections of the beam with the maximum stresses occurring at the fixed end. To produce a stress life curve simulations were performed at four different displacement amplitudes from 1.0 (μm) to 0.25 (μm). The simulations are performed through both the crack initiation and crack propagation stages so that the total life of the beam is obtained. The life of a particular beam versus the number of broken joints in the domain is shown in Figure 17. It can be seen in the figure that at a certain number of cycles a large number of joints break at once. This is the point at which catastrophic failure occurs and determines the total life of the component. The final crack pattern for the beam whose life is depicted in Figure 17 is shown in Figure 18. For this and many of the domains generated the first crack to develop often occurs at the corner where the vertical and horizontal sections meet due to the stress concentration that this union creates. For all of the cases considered the crack that propagated to failure occurred close to the fixed end. The lives of ten beams are found at each displacement amplitude. The stress versus life result is

shown in Figure 19. The stress values given along the ordinate are the maximum stresses that occur in the domain at each displacement amplitude.

Summary and Conclusions

This paper presents a damage mechanics based fatigue model to study the process of fatigue crack initiation and propagation in MEMS devices. The model takes into account the gradual material degradation that occurs under cyclic loading through an empirical damage evolution equation whose parameters are determined from fatigue testing of MEMS materials. The most important salient features of the proposed model include: a) the ability to predict the MEMS fatigue life over many hundreds of billions of cycles based on experimental data collected from a few million cycles; b) the ability to account for the statistical variation of the material properties; and c) the ability to account for material flaws caused by non-perfect fabrication techniques. The model is applied to a dog-bone shaped tensile specimen, a shape which has been commonly used in MEMS material testing, to investigate the effects of material heterogeneity and material flaws on fatigue life. Allowing for variability in the elastic and damage properties was found to lead to a similar increase in scatter and reduction in fatigue life. Much larger reductions in life and increases in scatter occurred when initial material flaws were considered. The largest increase in scatter and largest reduction in life occurred when there was an initial surface void. Stress life curves generated using the model showed fatigue lives scattered over more than two orders of magnitudes of cycles for some conditions. The ability of the model to predict the lives of different types of devices and loading conditions was demonstrated by generating the stress life curve for a MEMS resonator support beam.

Acknowledgement

The authors would like to express their deepest appreciations to DARPA MEMS/NEMS S&T fundamentals program and the IMPACT Center for their support of this research project.

References

[1] K.H.L. Chau and R.E. Sulouff, "Technology for the high-volume manufacturing of integrated surface-micromachined accelerometer products," *Microelectronics Journal*, vol. 29, pp. 579-586, 1998.

[2] D.R. Sparks, S.R. Zarabadi, J.D. Johnson, Q. Jiang, M. Chia, O. Larsen, W. Higdon, and P. Castillo-Borelley, "A CMOS integrated surface micromachined angular rate sensor: It's automotive applications," in *International Conference on Solid-State Sensors and Actuators Proceedings*, 1997, vol. 2, pp. 851-854.

[3] C.L. Goldsmith, D.I. Forehand, Z. Peng, J.C.M. Hwang, and J.L. Ebel, "High-cycle life testing of RF MEMS switches," in *IEEE MTT-S International Microwave Symposium Digest*, 2007, pp. 1805-1808.

[4] I. Chasiotis, "Mechanics of thin films and microdevices," *IEEE Transactions on Device and Materials Reliability*, vol. 4, no. 2, pp. 176-188, 2004.

[5] C.L. Muhlstein, S.B. Brown, and R.O. Ritchie, "High-cycle fatigue of polycrystalline silicon thin films in laboratory air," in *Materials Research Society Symposium Proceedings*, 2001, vol. 657, pp. EE581-EE586.

[6] H. Kahn, R. Ballarini, R.L. Mullen, and A.H. Heuer, Electrostatically actuated failure of microfabricated polysilicon fracture mechanics specimens," *Proceedings of the Royal Society of London*, vol. 455, pp. 3807-3823, 1999.

[7] H. Kapels, R. Aigner, and J. Binder, "Fracture strength and fatigue of polysilicon determined by a novel thermal actuator," *IEEE Transactions on Electron Devices*, vol. 47, pp. 1522-1528, 2000.

[8] J. Bagdahn and W.N. Sharpe, "Fatigue of polycrystalline silicon under long-term cyclic loading," *Sensors and Actuators A*, vol. 103, pp. 9-15, 2003.

[9] W.N. Sharpe and J. Bagdahn, "Fatigue testing of polysilicon – a review," *Mechanics of Materials*, vol. 36, no. 1-2, pp. 3-11, 2003.

[10] H. Kahn, R. Ballarini, and A.H. Heuer, "Dynamic fatigue of silicon," *Current Opinion in Solid State and Materials Science*, vol. 8, pp. 71-76, 2004.

[11] T.E. Buchheit, B.L. Boyce, and G.W. Wellman, "The Role of microstructure in MEMS deformation and failure," in *Proceedings of IMECE2002*, 2002, pp. 559-566.

[12] J. Aktaa, J.Th. Reszat, M. Walter, K. Bade, and K.J. Hemker, "High cycle fatigue and fracture behavior of LIGA nickel," *Scripta Materialia*, vol. 52, no. 12, pp. 1217-1221, 2005.

[13] Y. Yang, B.I. Imasogie, S.M. Allameh, B. Boyce, K. Lian, J. Lou, and W.O. Soboyejo, "Mechanisms of fatigue in LIGA Ni MEMS thin films," *Materials Science and Engineering A*, vol. 444, pp. 39-50, 2007.

[14] L.M. Kachanov, "Time of the rupture process under creep conditions," Izv Akad Nauk SSR, Otd Tekh Nauk, vol. 8, pp. 26-31, 1958.

[15] Y.N. Robotnov, *Creep Problems in Structural Mechanics*. North-Holland, 1969.

[16] J.L. Chaboche, "Continuum damage mechanics: Part I – general concepts," *Journal of Applied Mechanics*, vol. 55, pp. 59-64, 1988.

[17] N. Raje, F. Sadeghi, and R.G. Rateick Jr., "A discrete element approach to evaluate stresses due to line loading on an elastic half-space," *Computational Mechanics*, vol. 40, no. 3, pp. 513-529, 2007.

[18] A.V. Potapov, C.S. Campbell, and M.A. Hopkins, "A two-dimensional dynamic simulation of solid fracture Part I: description of the model," *International Journal of Modern Physics C*, vol. 6, no. 3, pp. 371-398, 1995.

[19] O. Ito and E.R. Fuller, "Computer modeling of anisotropic grain microstructure in two dimensions," *Acta Metallurgica et Materialia*, vol. 41, no. 1, pp. 191-198, 1993.

[20] P.D. Zavattieri and H.D. Espinosa, "Grain level analysis of crack initiation and propagation in brittle materials," *Acta Materialia*, vol. 49, pp. 4291-4311, 2001.

[21] J. Lemaitre, *A Course on Damage Mechanics*. Berlin: Springer-Verlag, 1992.

[22] V.V. Bolotin and I.L. Belousov, "Early fatigue crack growth as the damage accumulation process," *Probabilistic Engineering Mechanics*, vol. 16, pp. 279-287, 2001.

[23] J.L. Chaboche and P.M. Lesne, "A non-linear continuous fatigue damage model," *Fatigue and Fracture of Engineering Materials and Structures*, vol. 11, no. 1, pp. 1-17, 1988.

[24] Y.C. Xiao, S. Li, and Z. Gao, "A continuum damage mechanics model for high cycle fatigue," *International Journal of Fatigue*, vol. 20, no. 7, pp. 503-508, 1998.

[25] I. Rasool Memon, X. Zhang, and D. Cui, "Fatigue life prediction of 3-D problems by damage mechanics with two-block loading," *International Journal of Fatigue*, vol. 24, no. 1, pp. 29-37, 2002.

[26] V.V. Bolotin, *Mechanics of Fatigue*. Boca Raton: CRC Press, 1999.

[27] J. Bagdahn and W.N. Sharpe, "Fatigue of polycrystalline silicon under long-term cyclic loading," *Sensors and Actuators A*, vol. 103, pp. 9-15, 2003.

[28] S.M. Allameh, J. Lou, F. Kavishe, T. Buchheit, and W.O. Soboyejo, "An investigation of fatigue in LIGA Ni MEMS thin films," *Materials Science and Engineering A*, vol. 371, pp. 256-266, 2004.

[29] S.-W Kim, C.-S Oh, and H.-J Lee, "Specimen aligning techniques in tensile and fatigue tests for thin films," *Fatigue and Fracture of Engineering Materials and Structures*, vol. 30, no. 1, pp. 64-71, 2006.

[30] J.H. Park, S.H. Choa, H.C. Choi, M.S. Myung, C.S. Lee, and Y.J. Kim, "Fatigue test of Al-3% TI using axial loading testing machine for MEMS materials," in *Proceedings of IPACK* 2005, 2005, pp. 1725-1730.

[31] W.D. Callister, *Materials Science and Engineering an Introduction*. New York: John Wiley & Sons, 2000.

[32] A. McCarty and I. Chasiotis, "Description of brittle failure of non-uniform MEMS geometries," *Thin Solid Films*, vol. 515, pp. 3267-3276, 2007.

[33] D.C. Miller, B.L. Boyce, M.T. Dugger, T.E. Buchheit, and K. Gall, "Characteristics of commercially available silicon-on-insulator MEMS material," *Sensors and Actuators A*, vol. 138, pp. 130-144, 2007.

[34] T.E. Buchheit, S.J. Glass, J.R. Sullivan, S.S. Mani, D.A. Lavan, T.A. Friedmann, and R. Janek, "Micromechanical testing of MEMS materials," *Journal of Materials Science*, vol. 38, pp. 4081-4086, 2003.

[35] D.A. LaVan, B.L. Boyce, and T.E. Buchheit, "Size and frequency of defects in silicon MEMS," in *Proceedings of IMECE2002*, 2002, pp. 573-576.

[36] M.J. Madou, *Fundamentals of Microfabrication: The Science of Miniaturization*. CRC; 2nd edition, 2002.

[37] G.M. Rebeiz, *RF MEMS: Theory, Design, and Technology*. Wiley-Interscience, 2002.

[38] S.S. Senturia, *Microsystem Design*. Springer; 2nd edition, 2004.

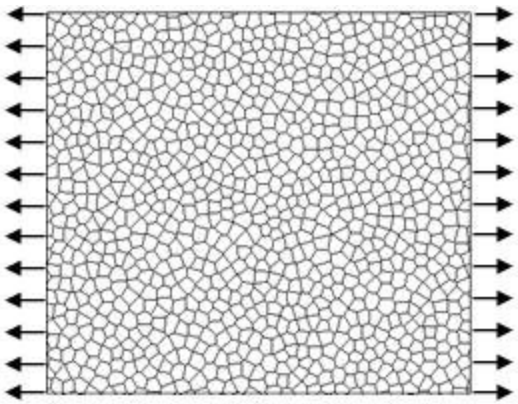

Figure 1: A solid formed by a collection of discrete elements subjected to an applied external boundary loading.

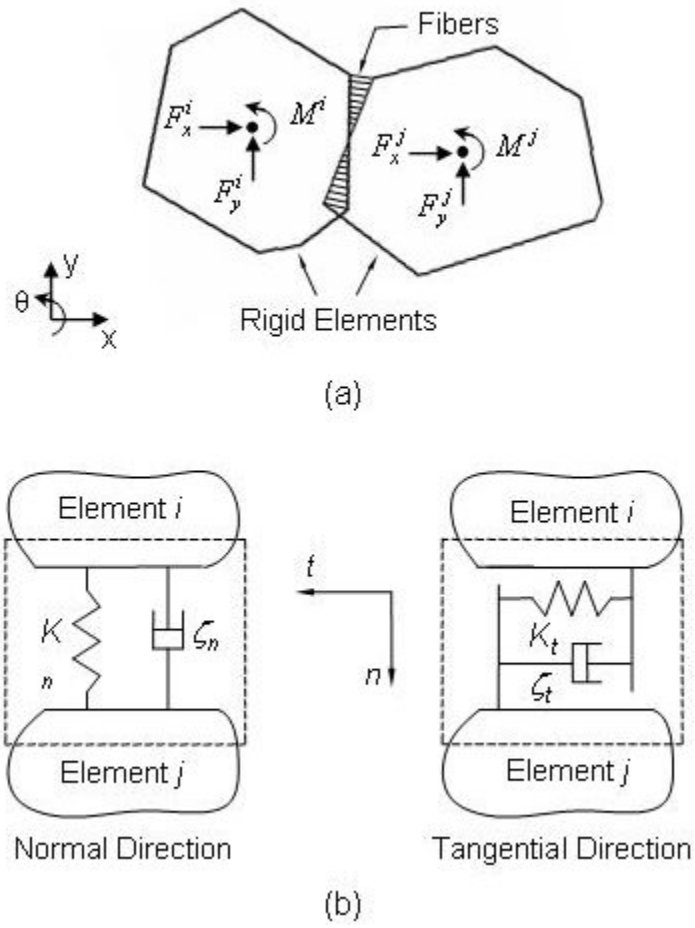

Figure 2: (a) Inter-element contact in the discrete model; (b) Fiber model.

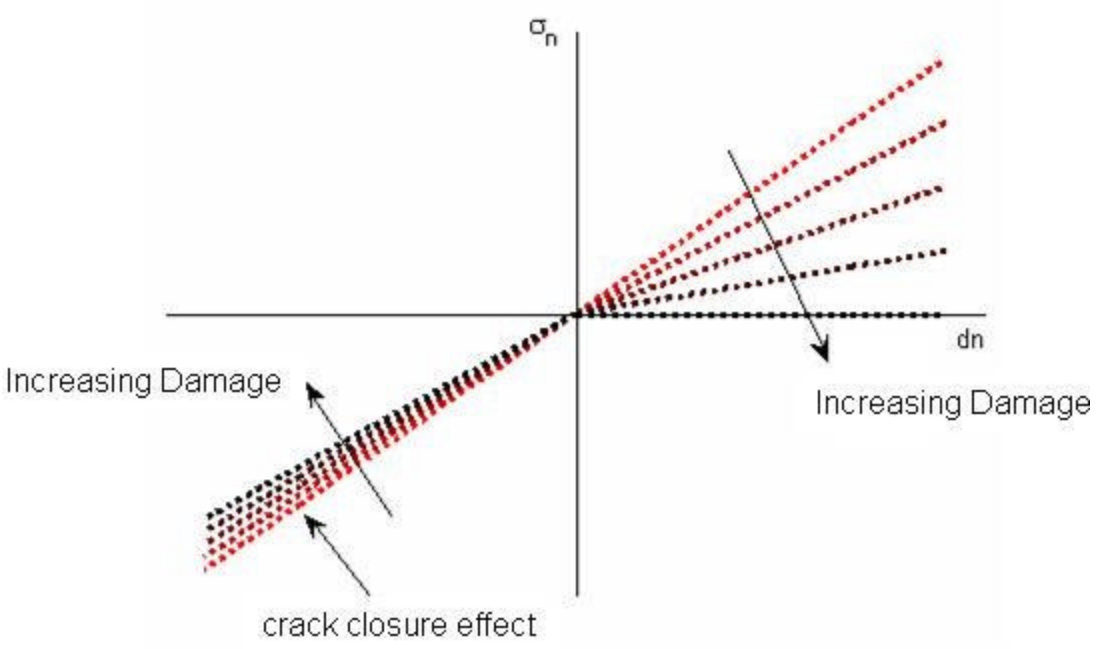

Figure 3: Degradation of joint normal stiffness with damage accumulation.

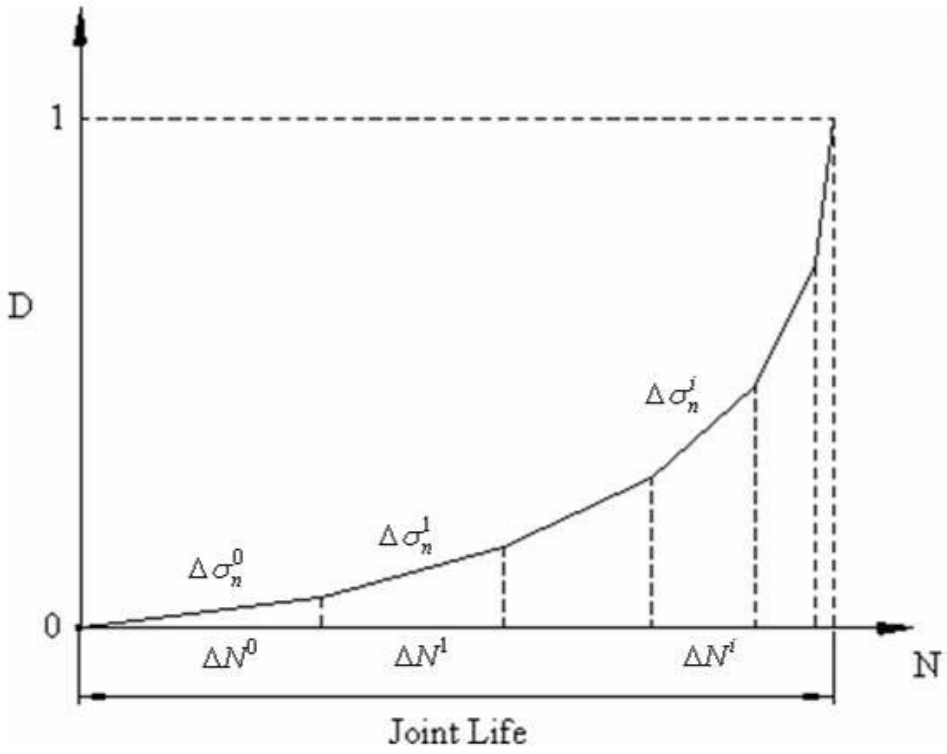

Figure 4: Piecewise linear approximation for damage evolution.

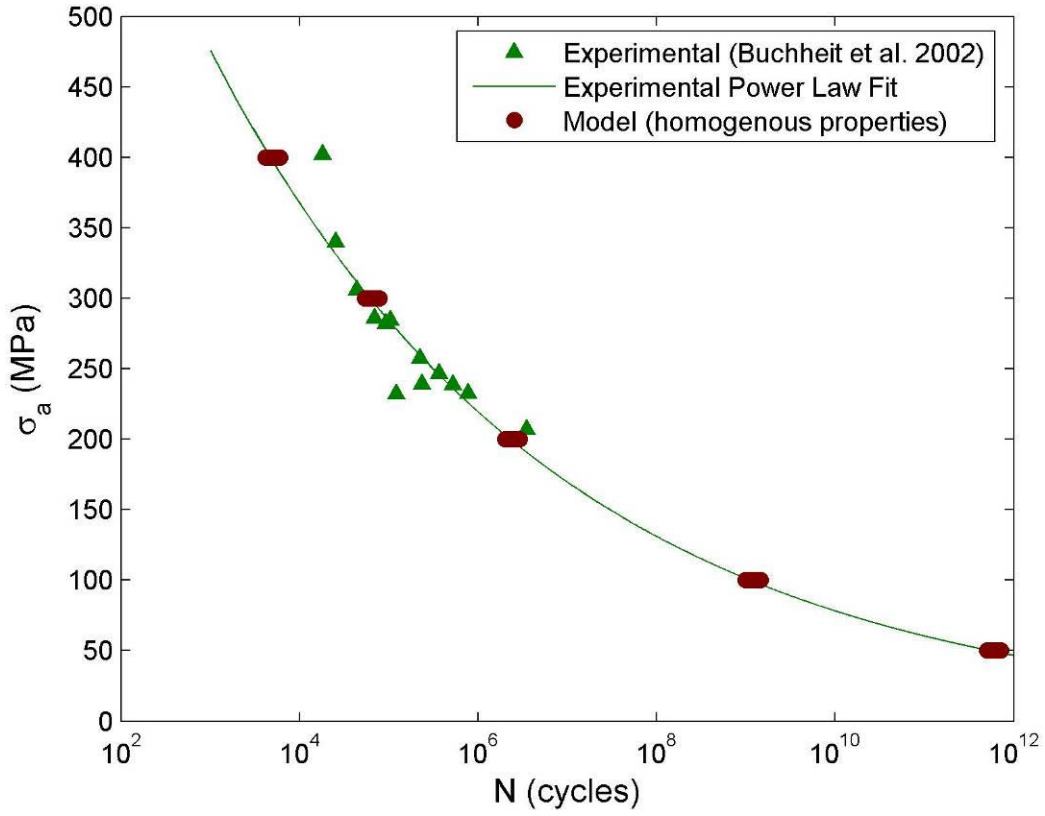

Figure 5: S-N curve for LIGA Ni, Buchheit [3].

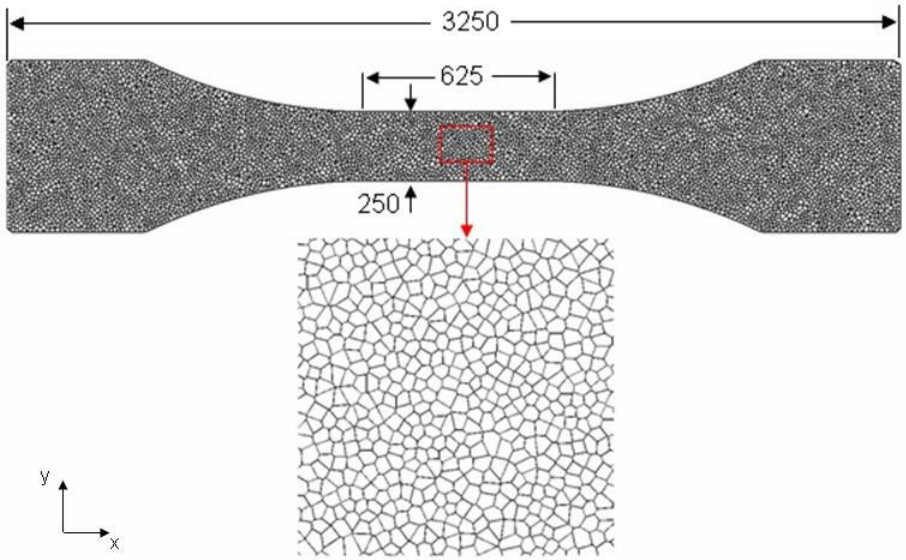

Figure 6: Fatigue specimen modeled using the discrete element based material model. Dimensions are given in micrometers.

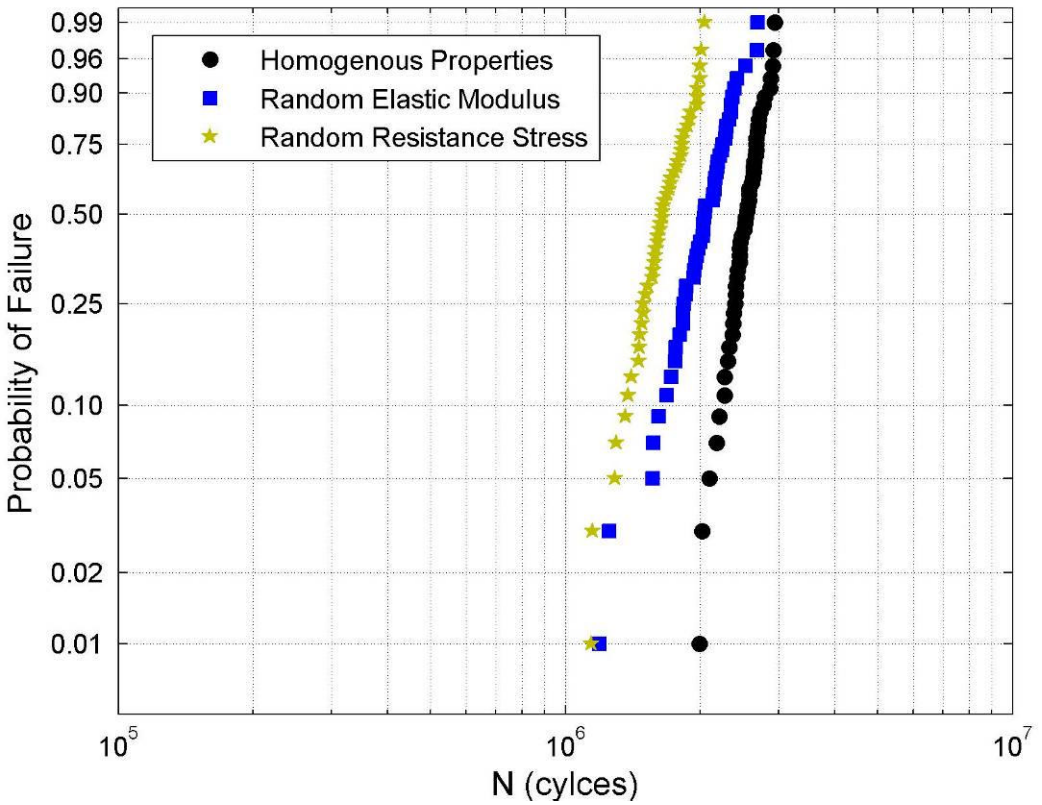

Figure 7: Weibull life plot for crack initiation in fifty different domains subjected to different material property conditions.

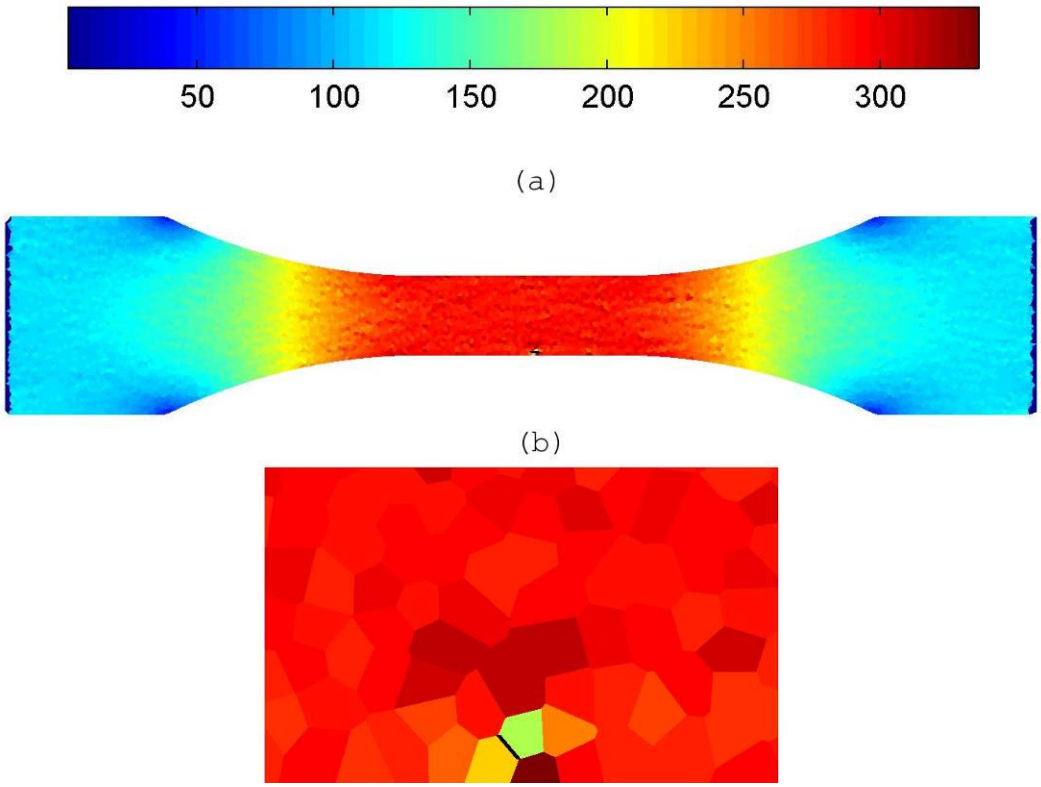

Figure 8: Von Mises stress distribution in a tensile specimen with one initial broken bond for a stress amplitude of 300 MPa.. (b) Close up view of the stress distribution around the initial broken bond represented by the black line. The stress values are given in MPa.

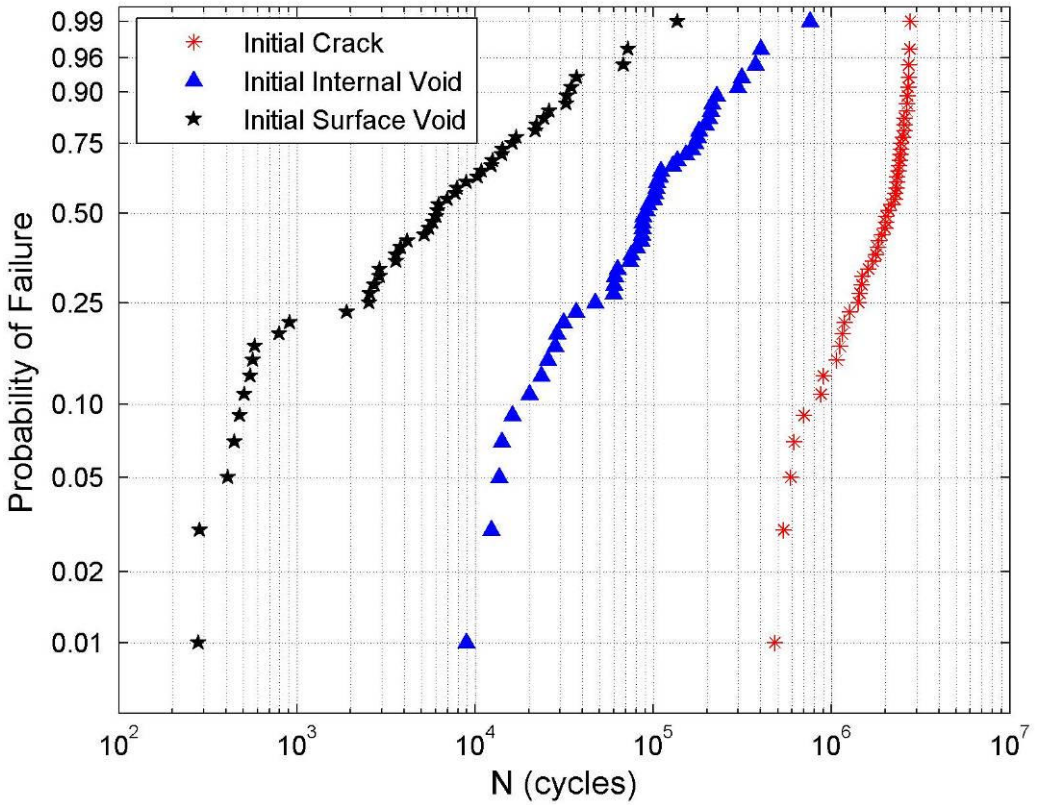

Figure 9: Weibull life plot for crack initiation in fifty different domains with initial flaws.

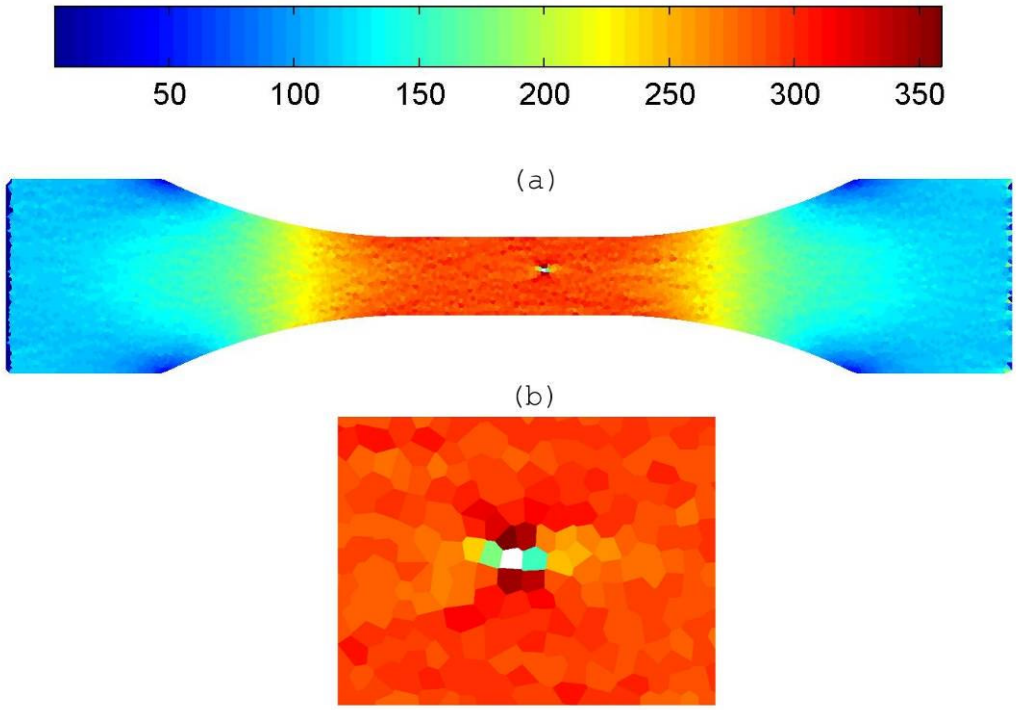

Figure 10: Von Mises stress distribution in a tensile specimen with one initial internal void for a stress amplitude of 300 MPa. (b) Close up view of the stress distribution around the void. The stress values are given in MPa.

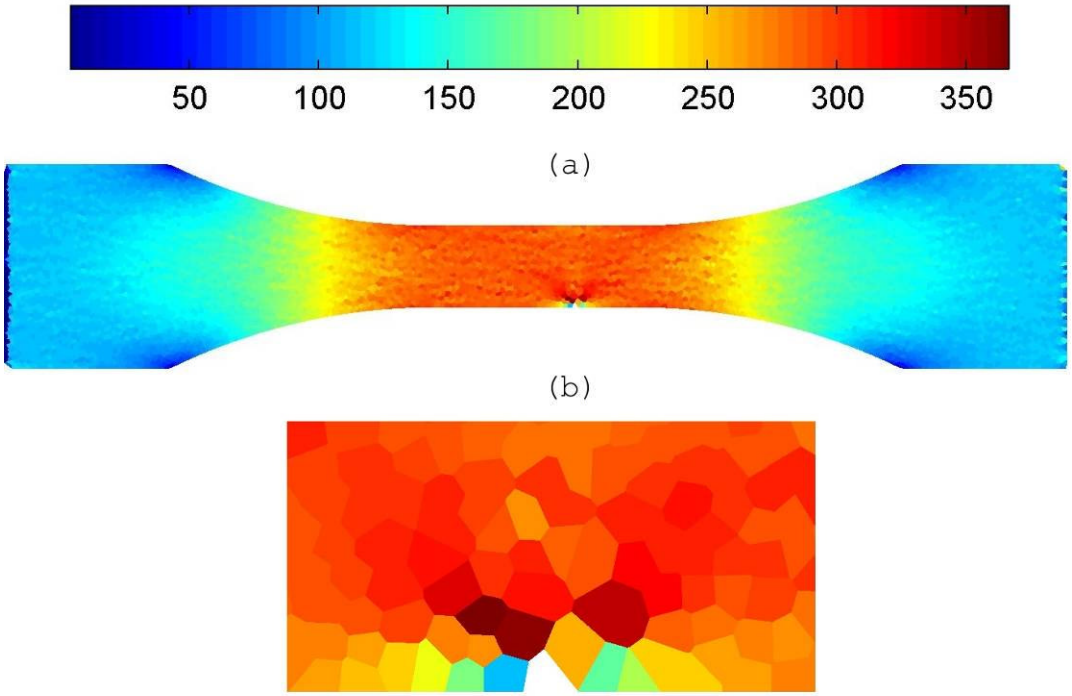

Figure 11: Von Mises stress distribution for a tensile specimen with one initial surface void for a stress amplitude of 300 MPa.. (b) Close up view of the stress distribution around the initial surface void. The stress values are given in MPa.

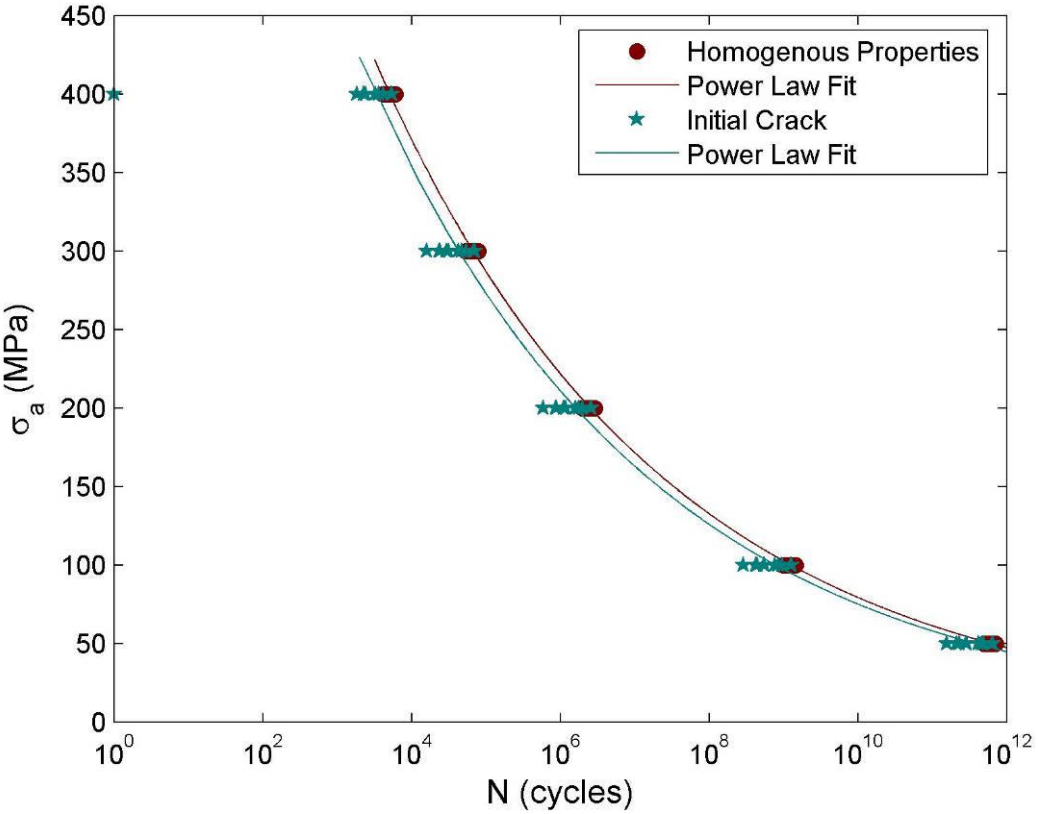

Figure 12: S-N curve for crack initiation in a tensile specimen with one initial crack.

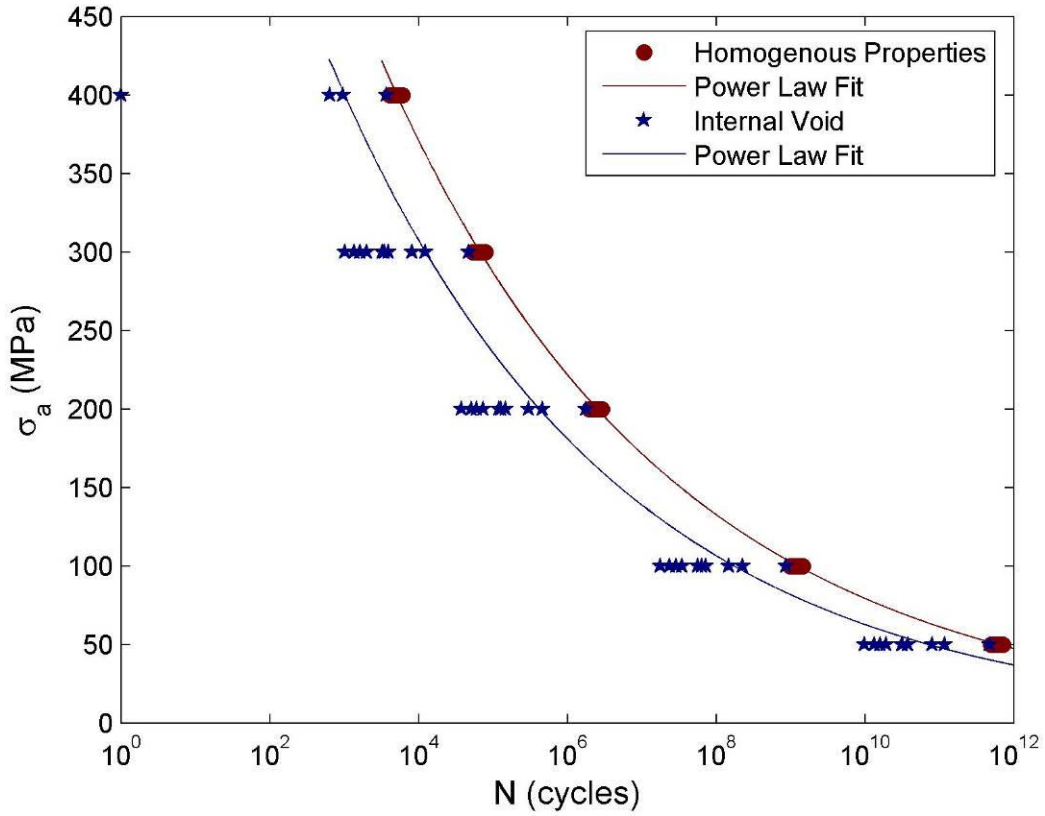

Figure 13: S-N curve for crack initiation in a tensile specimen with one initial internal void.

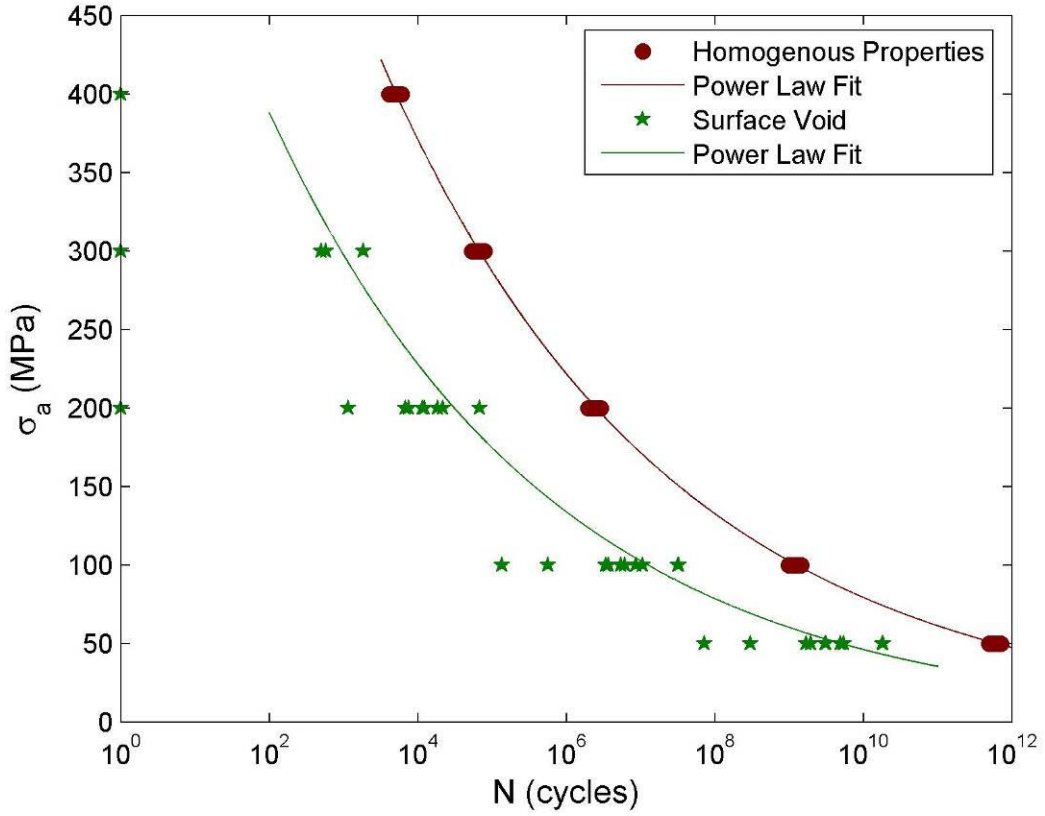

Figure 14: S-N curve for crack initiation in a tensile specimen with one initial surface void.

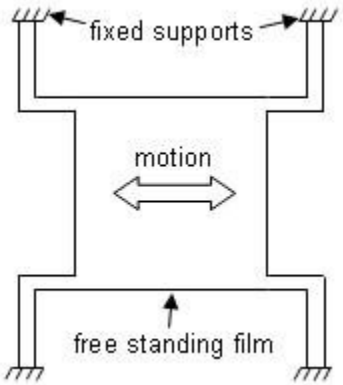

Figure 15: MEMS Resonator

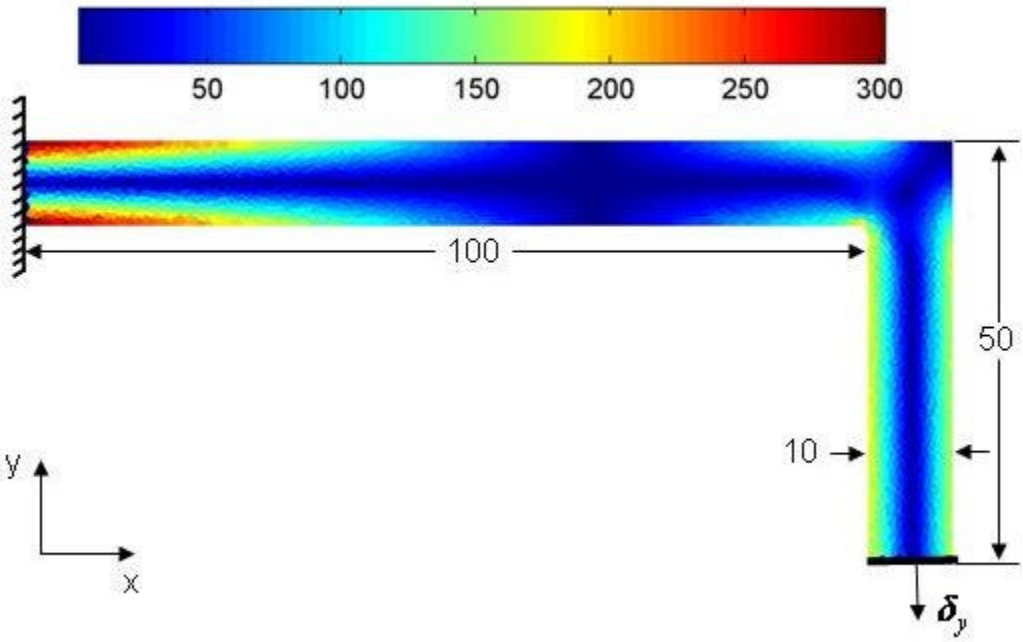

Figure 16: Von Mises stress distribution in a MEMS resonator support beam subjected to a δ_y = 1.0 (μm) displacement. Dimensions are in micrometers. The stress values are given in MPa.

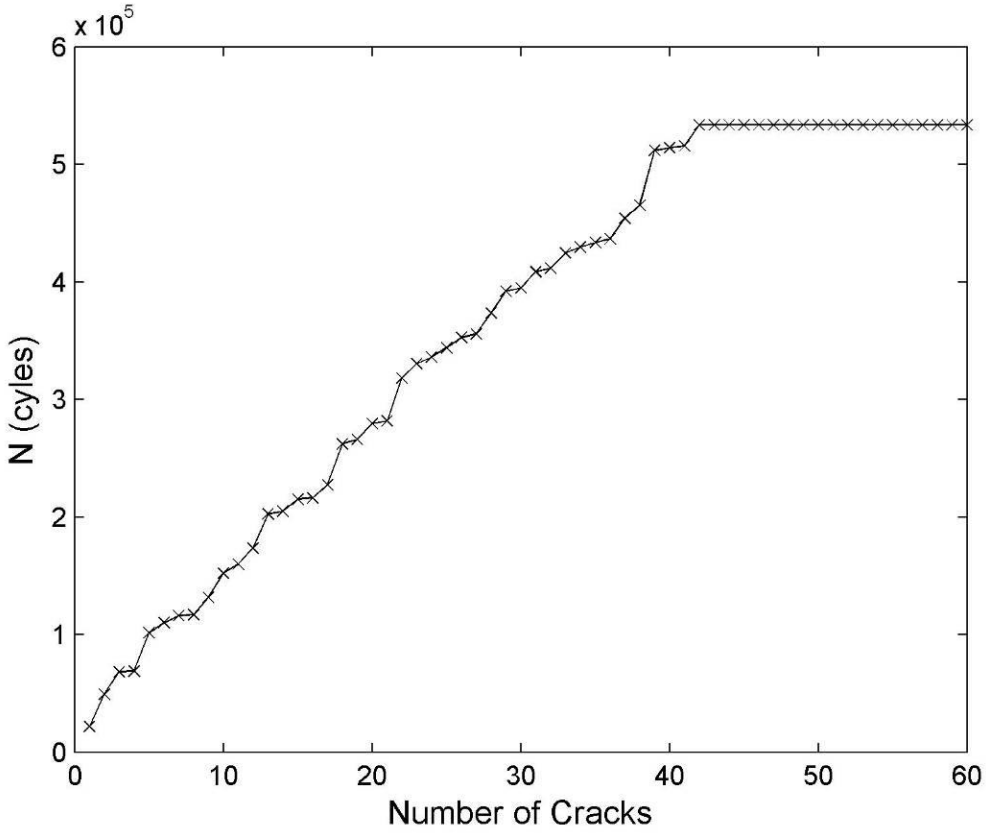

Figure 17: Fatigue life versus the number of cracks in the beam supporting structure for a particular domain.

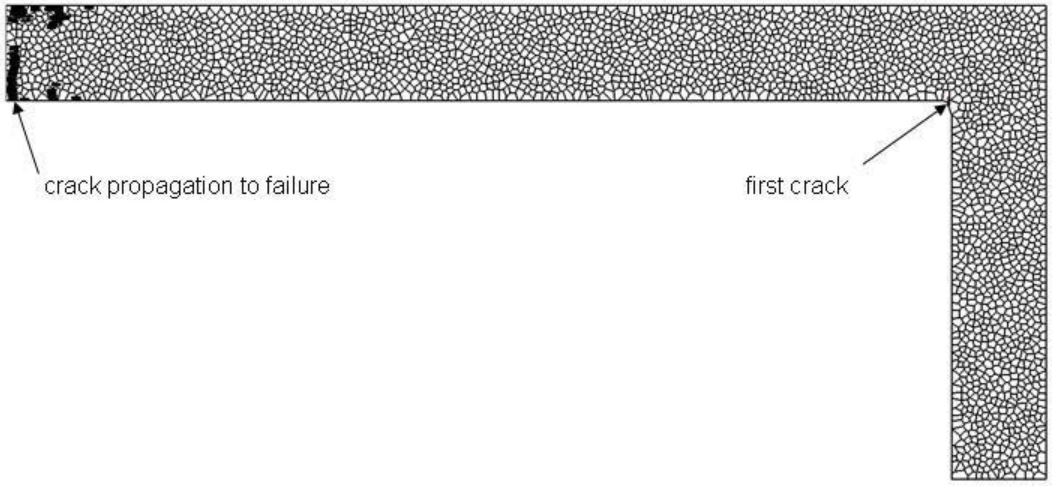

Figure 18: Crack propagation pattern in MEMS resonator support beam.

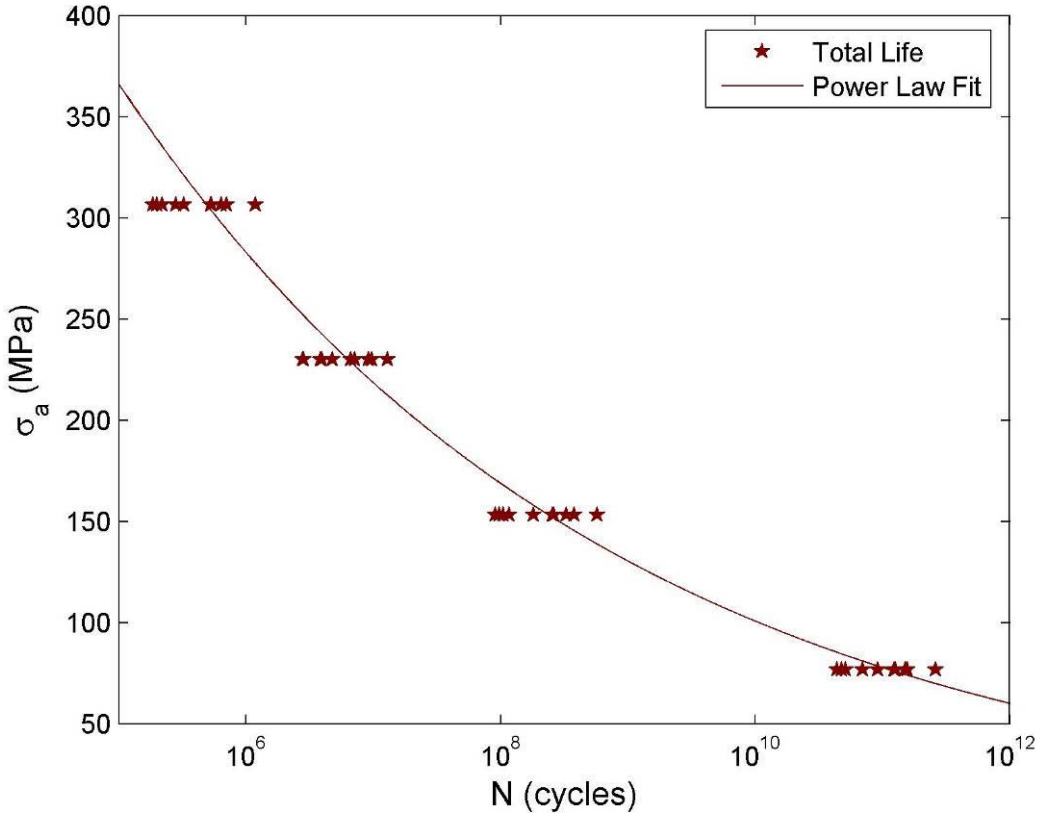

Figure 19: S-N curve for the total life of a MEMS resonator support beam.